Modeling Lunar Pyroclasts to Probe the Volatile Content of the Lunar Interior

Darien Florez[1], Christian Huber[1], Ralph Milliken[1], Julia Berkson[1]

[1]Brown University, Department of Earth, Environmental and Planetary Sciences
Contact: darien_florez@brown.edu

1. Abstract

Constraining the volatile budget of the lunar interior has important ramifications for models of Moon formation. While many early and previous measurements of samples acquired from the Luna and Apollo missions suggested the lunar interior is depleted in highly volatile elements like H, a number of high-precision analytical studies over the past decade have argued that it may be more enriched in water than previously thought. Here, we integrate recent remotely sensed near-infrared reflectance measurements of several Dark-Mantle-Deposits (DMDs), interpreted to represent pyroclastic deposits, and physics-based eruption models to better constrain the pre-eruptive water content of lunar volcanic glasses. We model the trajectory and water loss of pyroclasts from eruption to deposition, coupling eruption dynamics with a volatile diffusion model for each pyroclast. Modeled pyroclast sizes and final water contents are then used to predict spectral reflectance properties for comparison with the observed orbital near-infrared data. We develop an inversion scheme based on the Markov-Chain Monte-Carlo (MCMC) method to retrieve constraints between governing parameters such as the initial volatile content of the melt and the pyroclast size distribution (which influences the remotely measured water absorption strengths). The MCMC inversion allows us to estimate the primordial (pre-eruption) water content for different DMDs and test whether their source is volatile-rich. Our results suggest that the parts of the lunar interior sampled by the source material of the DMDs investigated in this study range in water content from 400 to 800 ppm.

2. Introduction

Volatile elements, in particular hydrogen (e.g., in the form of OH/H_2O, hereafter referred to simply as 'water' or H_2O), affect planetary processes via their control over magma viscosity, mineral stability, and magma eruption dynamics [*Asimow et al.*, 2003; *Gaetani and Grove*, 1998; *Hirth and Kohlstedt*, 1996].

Although several different competing models exist, several models of lunar formation that have recently gained momentum in the planetary science community involve to an extent the giant impact theory (see, for example, the terrestrial synestia model of *Lock et al.* [2018]). In this giant impact theory, the Moon is thought to have been formed from the coalescence of debris from a collision between an impactor and a proto-Earth [*Canup*, 2004], leading to the formation of a lunar magmatic ocean and the large-scale degassing of the Moon [*Lucey et al.*, 2006]. The depletion of water in volcanic samples returned from Luna and Apollo missions seemed to support this, but a growing body of research now suggests that the lunar mantle, or at least some parts of the lunar mantle, may not be as severely depleted in water as previously thought [*Boyce et al.*, 2010; *Greenwood et al.*, 2011; *Hauri et al.*, 2011; *Hui et al.*, 2017; *McCubbin et al.*, 2010a; *McCubbin et al.*, 2010b; *Rutherford et al.*, 2017; *Saal et al.*, 2008; *Saal et al.*, 2013].

Much of the uncertainty surrounding the character of the lunar interior stems from the availability of direct samples from the lunar surface being limited to only a small number of locations. However, telescopic and other remote sensing observations have revealed so-called

Dark Mantle Deposits (DMDs) to be distinct features across the lunar surface [*L Gaddis et al.*, 1998; *L R Gaddis et al.*, 2000; *L R Gaddis et al.*, 1985; *L R Gaddis et al.*, 2003; *Gustafson et al.*, 2012; *Head*, 1974; *Weitz et al.*, 1998]. Although no large DMD has ever been sampled, and in general their relation to the specific pyroclastic materials returned from the Luna and Apollo missions is unclear, they are interpreted to be pyroclastic in nature and, if true, represent magmas sourced from the deep lunar interior [*L R Gaddis et al.*, 1985; *Head*, 1974; *Weitz et al.*, 1998].

Most recent work using lunar samples to robustly constrain the water content of the lunar interior has focused on picritic glasses [*Hauri et al.*, 2011; *Rutherford et al.*, 2017; *Saal et al.*, 2008; *Saal et al.*, 2013]. These glasses are thought to have been emplaced through Hawaiian-like, fire-fountaining eruptions [*Wilson and Head III*, 2003] and include green (low Ti), yellow (intermediate Ti), and orange, red, and black glasses (high Ti). They represent quenched melts that are ultramafic in composition [*J W Delano*, 1986; *Saal et al.*, 2008], crystal poor [*J W Delano*, 1986; *Saal et al.*, 2008], were erupted as fine beads (< 1 mm) [*J W Delano*, 1986; *G Heiken and McKay*, 1977; *Longhi*, 1992; *Saal et al.*, 2008; *Weitz et al.*, 1998], and are believed to have been generated from magmas sourced at depths of 300 - 500 km [*J Delano*, 1980; *J Delano and Lindsley*, 1983; *Elkins et al.*, 2000; *Elkins-Tanton et al.*, 2003; *Longhi*, 2006; *C Shearer and Papike*, 1993; *C K Shearer et al.*, 2006]. For this reason, they have been used to probe the volatile content of parts of the lunar interior by virtue of melt inclusions, diffusion modeling, and through solubility experiments [*Hauri et al.*, 2011; *Rutherford et al.*, 2017; *Saal et al.*, 2008; *Saal et al.*, 2013].

Volatile content profiles of individual picritic glass beads were first reported by *Saal et al.* [2008], where improvements in secondary ion mass spectrometry allowed for lower detection threshold for water. These improvements led to the detection of measurable amounts of water (up to 46 ppm), and *Saal et al.* [2008] found systematic depletion from core to rim within individual beads. These volatile profiles suggest the beads degassed during ascent and eruption [*Saal et al.*, 2008], consistent with a volcanic (as opposed to impact) origin. The trace amount of water detected in these glasses therefore represents the concentration of water in the parental magma upon fragmentation after magmatic degassing.

Magmatic degassing is assumed to take place as fragmented pyroclasts travel through a thermally opaque, water undersaturated, gas cloud during their ballistic trajectory [*Wilson and Keil*, 2012]. The volatile profiles recorded by these pyroclasts during this process are therefore modulated by the cooling time (i.e. the time spent traveling through the opaque gas cloud), the size and shape of the pyroclast, and the pre-eruption magmatic volatile content, as well as the conditions (rate) above the blocking temperature [*Crank*, 1975]. Here, the blocking temperature is generally assumed to be the melt-glass transition temperature for the volatile species considered. Based on these relationships, the volatile profiles measured in the pyroclasts can be used to constrain the range of values for these different parameters. For instance, *Saal et al.* [2008] applied the measured volatile content values to a degassing/diffusion model and estimated the initial amount of water upon magma fragmentation to be within the range of 260 to 15,000 ppm [*Saal et al.*, 2008] (94.0% and 99.9% percent water loss, respectively), with a best-fitting solution of 745 ppm (98% water loss). Though even the lowest model values have a significant implication for the volatile budget of the Moon, this is a broad range and the solution is clearly not unique. Therefore, further constraints are desired to help narrow down the range of possible

solutions and provide useful estimates of mantle volatile composition in the source magmas that feed pyroclastic eruptions on the Moon.

One useful additional constraint is, when possible, to locate the vent(s) associated with a pyroclastic deposit. The size of a pyroclastic deposit and the distance from the point of origin (vent) provides information on the trajectory of the pyroclasts and thus their cooling time above the blocking temperature. Unfortunately, specific vents associated with glass beads returned from the Luna and Apollo sampling sites are not apparent in existing data. However, remotely sensed data such as images from NASA's Lunar Reconnaissance Orbiter have revealed the presence of vents for several small DMDs elsewhere on the lunar surface [*Gustafson et al.*, 2012]. In addition, near-infrared reflectance spectra acquired by the Moon Mineralogy Mapper (M3) imaging spectrometer on the Chandrayaan-1 spacecraft have revealed that nearly all DMDs on the Moon exhibit spectral signatures indicative of enhanced water contents, including several of the small DMDs with visible vents [*Li and Milliken*, 2017; *Ralph E Milliken and Li*, 2017].

The M3 reflectance spectra, in conjunction with laboratory measurements and radiative transfer models, were used to estimate the amount of water in the DMDs based on the strength of an OH/H2O absorption feature at a wavelength of ~2.7-2.9 μm [*Ralph E Milliken and Li*, 2017]. The parameter used to characterize the absorption strength was the Effective Single Particle Absorption Thickness (ESPAT) as described and defined by [*Hapke et al.*, 1993]. Previous studies have shown that the ESPAT parameter is linearly correlated with water content for a wide range of hydrous materials, but the slope of that linear relationship varies with the particle size of the material [*Li and Milliken*, 2017; *Ralph Edward Milliken*, 2006; *Ralph E Milliken and Mustard*, 2005; 2007a; b]. In order to estimate the current (post-emplacement) water content of the DMDs, *Ralph E Milliken and Li* [2017] assumed the deposits were spectrally dominated by particles (pyroclasts) ~60-80 μm in diameter. The main challenges with this approach are (1) that the pyroclast size distribution of the deposits as a whole, as well as the pyroclast size distribution with distance from the vent, are unknown, and (2) that volatile diffusion profiles for glass beads within these deposits are unavailable and therefore can't be used to independently determine the pre-fragmentation water content.

In this study we seek to determine if there exist a suite of conditions for which analytical measurements of lunar glasses, physical eruption models, and remotely sensed measurements of pyroclastic deposits yield self-consistent results for water in lunar DMDs. That is, can pyroclast size distributions and water content values estimated from an eruption model be used to predict the range of possible absorption strengths (ESPAT values) that might be observed in near-infrared reflectance spectra and are these in agreement with the values reported in Milliken and Li (2017)? Alternatively, do eruption models predict pyroclast sizes significantly larger or smaller than assumed in that previous study and, if so, what does this imply about quantifying water content of DMDs using near-infrared reflectance data such as M^3? To address these issues and further constrain pre-fragmentation water content of lunar magmas, we develop a new approach using eruption dynamics together with volatile diffusion out of pyroclasts. Near-IR ESPAT values are expected to vary as a function of both water content and pyroclast size [*Li and Milliken*, 2017; *Ralph E Milliken and Li*, 2017]. As such, transects of ESPAT values from a DMD vent to its perimeter are expected to vary based on differences in pre-fragmentation water content, pyroclast size, and the exsolved gas content that accelerates the pyroclasts to their

eventual deposition. All three of these critical parameters can be independently evaluated in a physics-based eruption model, and we use ESPAT profiles measured across several small DMDs with vents to find a solution space that results in fits to the ESPAT profiles while simultaneously satisfying the dynamics of large fire fountain volcanic events on the Moon. To accomplish this, we develop an approach that requires calculating water loss through magmatic diffusion in pyroclasts and the loss is calculated here using new constraints from diffusion modeling of analytically measured picritic glasses similar to that of *Saal et al.* [2008]. This study represents the first time that analytical measurements of lunar glasses, a physics-based eruption model, and remote sensing observations of lunar water absorptions have all been integrated to better constrain the amount of water in lunar DMDs and their magma source regions.

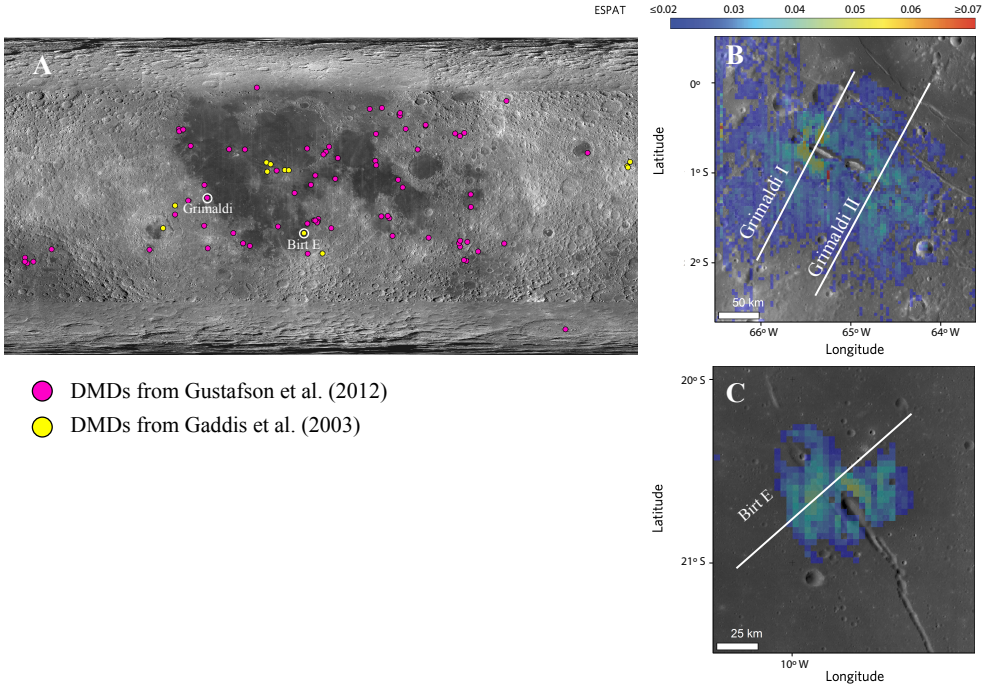

Figure 1. A Map of Dark Mantle Deposits (DMDs) in and around Procellarum Kreep Terrain identified from *Gustafson et al.* [2012] and *L R Gaddis et al.* [2003]. DMDs Grimaldi and Birt E (investigated in this study) are circled in white. **B + C** ESPAT maps and approximate transect lines of DMDs Grimaldi and Birt E, respectively.

3. Methods

To investigate the volatile budget of DMD source material, we couple an eruption model for pyroclast dispersal with a diffusion model to account for volatile loss during pyroclast transport above the blocking temperature. The pyroclast sizes and water contents that are output by the model are used to predict the near-IR ESPAT values that would be observed in the M3 data (described in detail below), where the ESPAT values are a quantitative measure of the OH/H_2O absorption strength near a wavelength of ~2.9 μm and whose derivation is described in *Ralph E Milliken and Li* [2017] and *Li and Milliken* [2017]. We use maps of ESPAT values previously published by *Ralph E Milliken and Li* [2017] and *Li and Milliken* [2017] to extract transects of ESPAT values over two small DMDs with identifiable vents: Birt E and Grimaldi [*Ralph E Milliken and Li*, 2017] (**figure 1**). The eruption dynamics model solves for the depth of magma fragmentation, which depends on the exsolved volatile content of the magma rising to the surface, and the ballistic trajectory of *n* pyroclasts of a certain size (diameter) distribution and pre-eruptive water content. The volatile loss experienced by each of the *n* pyroclasts is calculated

with a diffusion model calibrated on the data of *Saal et al.* [2008]. This allows us to generate a map of pyroclast size and post-diffusion water content as function of distance from the vent and thus construct synthetic ESPAT value maps for the two DMDs. The free parameters in the model are the pre-fragmentation water content of the rising magma, the concentration of exsolved volatiles at fragmentation, and pyroclast size distribution. The misfit between the synthetic (modeled) and measured ESPAT values of the DMD's are calculated and a Markov-Chain Monte-Carlo is implemented in order to retrieve the parameters that result in the best models (i.e. the most probable model parameters). Although the actual areal extent and even the corresponding source vents of many lunar DMDs may be obscured by younger mare deposits [*Head*, 1974], the inversion is preformed such that the model fits the entire ESPAT transect, and thus makes no assumptions of the deposit size other than that it is smaller than the length of the transect itself. Using this technique, we can ascertain the most probable pre-eruptive water content, concentration of exsolved gas upon fragmentation, as well as pyroclast size distribution parameters that reproduce the observed water absorption strengths (ESPAT values) for the deposits of interest. Definitions for all variables used by the model are provided in **table 1** below.

Symbol	Definition	Units
n_{H2O}	mass fraction of pre-fragmentation water	
n_{gas}	mass fraction of exsolved volatiles at fragmentation	
μ	mean pyroclast size	ϕ
σ	pyroclast size standard deviation	ϕ
d	diameter of pyroclast	m
$\bar{d}$	average pyroclast size of deposit	m
R	radius of pyroclast	m
Q_u	universal gas constant, 8.314×10^3	J $kmol^{-1}$ K^{-1}
ρ_l	density of picritic magma	kg/m^3
m	molar mass of exsolved gas at fragmentation	kg/kmol
T_m	temperature of melt	K
P_{frag}	fragmentation pressure	Pa
P_{ch}	choked flow pressure at vent	Pa
U_v	vent velocity of gas and perfectly coupled pyroclasts	m/s
P_f	final pressure gas expands to	Pa
N_a	Avogadro's number	mol^{-1}
ϕ_{gas}	effective gas molecule diameter, $\sim 3.4 \times 10^{-10}$	m
U_f	velocity of gas and perfectly coupled particles at P_f	m/s

u_t	terminal velocity of pyroclasts	m/s
U_b	initial ballistic velocities for pyroclasts	m/s
X	dimension of thermally opaque gas cloud	m
R_f	maximum range for pyroclastic deposit	m
F_e	erupted volume flux of magma from fissure vent	m^3/s
t_{dike}	total time pyroclasts spend in dike post fragmentation	s
t_{cloud}	total time pyroclasts spend in gas cloud post dike	s
t_{total}	total time pyroclasts spend diffusing	s
C^i	concentration of volatile species *i*	ppm
β^i	evaporation rate for chemical species *i*	m/s
D^i	temperature dependent diffusivity for chemical species *i*	m^2/s
D_o^i	diffusion coefficient for chemical species *i*	m^2/s

Table 1. Table summarizing symbols for coefficients used in model calculations.

2.1 Eruption model

We simulate the eruption and deposition of *n* pyroclasts using the eruption model of *Wilson et al.* [2010], *Wilson and Keil* [2012], *Wilson and Head III* [2003], *Wilson and Head* [2017], and *Head and Wilson* [2017], with model parameters **m**. Here, **m** can be written as:

$$\boldsymbol{m} = \left[n_{H_2O}, n_{gas}, \mu, \sigma\right] \quad (1)$$

where n_{H_2O} is the initial concentration of H_2O in DMD parental magma upon fragmentation, n_{gas} is the concentration of the mixture of exsolved gas driving the eruption upon fragmentation, and μ and σ are the mean and standard deviation of the pyroclast size distribution. Here μ and σ are expressed in terms of Φ, where Φ is related to pyroclast size diameter, d, in mm as [*Krumbein*, 1934; *Mueller et al.*, 2019]:

$$d = 2^{-\Phi} . \quad (2)$$

Using a lognormal relationship between Φ and wt% as implemented by *Mueller et al.* [2019], we generate a pyroclast size distribution for *n* pyroclasts (*n* = 40,000 for simulations presented in **table 2***)*. Given pyroclast size parameters μ and σ, representing the mean and standard deviation of the deposit in terms of Φ, the fraction of the arbitrary population that any given pyroclast size comprises and the resulting average pyroclast size can be calculated.

The composition of the gas mixture exsolved from lunar picritic magmas upon fragmentation are best constrained using melt inclusion and glass data, as well as solubility experiments performed

on orange (high-Ti) lunar glass beads [*Fogel and Rutherford*, 1995; *Rutherford et al.*, 2017; *Wetzel et al.*, 2015; *Wetzel et al.*, 2013]. These studies suggest that the orange picritic glasses fragmented at a depth of 300 – 600 m, based on considerations of the concentration of C dissolved in melt inclusions. Taking this into account, we use the composition of the exsolved gas phase of the picritic magma at depths of 300 – 600 m, as calculated by *Rutherford et al.* [2017] corresponding to 115 ppm CO, 10 ppm H_2O, 18 ppm S_2, 34 ppm SO_2, 19 ppm H_2S, and 10 ppm F.

To solve for the pyroclasts' trajectory, we first calculate the pressure (and depth) at which the rising magma is disrupted and transitions from a melt with suspended gas into a gas with suspended melt droplets by assuming a critical volume fraction of gas as 0.85 using the ideal gas law:

$$P_{frag} = \frac{0.15\, n_{gas}\, Q_u\, T_m\, \rho_l}{0.85(1-n_{mix})m} \quad (3)$$

where P_{frag} is the disruption pressure, n_{gas} is the mass fraction of exsolved volatiles, Q_u is the universal gas constant (8.314kJ $kmol^{-1}$ K^{-1}), T_m is the magmatic temperature, ρ_l is the density of the liquid phase, and m is the molar mass of the volatile mixture [*Wilson and Head*, 2017]. The magmatic temperature here is assumed to be 1450 ºC, slightly above the maximum liquidus of the green picritic glasses which ranges from 1405 to 1448 ºC [*J Delano*, 1990]. This assumption is supported by the fact that most picritic glasses tend to be crystal poor [*Elkins-Tanton et al.*, 2003].

The pyroclasts are assumed to be perfectly coupled to the gas and therefore travel and accelerate with the gas as it expands to the choked flow conditions at the vent, P_{ch}, which can be calculated iteratively as *Wilson and Head* [2017]:

$$\frac{n_{gas}\, Q_u\, T_m}{m} \ln\frac{P_{frag}}{P_{new}} + \frac{1-n_{gas}}{\rho_l}(P_{frag} - P_{old}) = P_{old}^2 \frac{m}{2\, n_{gas}\, Q_u\, T_m} \frac{n_{gas}\, Q_u\, T_m}{m\, P_{old}} + \frac{1-n_{gas}^2}{\rho_l} \quad (4)$$

With knowledge of the pressure of disruption and the pressure at the vent from Eq. (4), the total time that the newly formed pyroclasts spend at high temperatures while being transported in the dike/conduit, t_{dike}, can be calculated using the Simpson integration rule [*Atkinson*, 1989] and integrating from the fragmentation depth to the surface.

From P_{ch} obtained from Eq. (4), the averaged vent velocity, U_v, can be approximated as:

$$0.5\, U_v^2 = \frac{n_{gas}\, Q_u\, T_m}{m} \ln\frac{P_{frag}}{P_{ch}} + \frac{1-n_{gas}}{\rho_l}\left(P_{frag} - P_{ch}\right) - \left(\frac{P_{frag}-P_{ch}}{\rho_c}\right) \quad (5)$$

using the arguments from *Wilson* [1980] and *Wilson and Head* [2017], where ρ_c is the density of the lunar crust, 2550 kg m^{-3} [*Wieczorek et al.*, 2013]. Next, the final pressure, P_f, at which the gas expands to outside of the vent can be calculated using Eq. (6), which depends on the average pyroclast size of the eruption [*Wilson and Head*, 2017; *Wilson et al.*, 2010]. Pyroclasts that are

perfectly coupled will inherit the velocity of the gas as it expands to P_f, where P_f is calculated as [*Wilson and Head*, 2017; *Wilson et al.*, 2010]:

$$P_f = \frac{2^{0.5}\, Q_u\, T_m}{3\,\pi\,\varphi^2\, N_a\, \bar{d}} \quad (6)$$

where φ is the effective diameter of the gas molecules, 3.4×10^{-10} m for CO, $\bar{d}$ is the average pyroclast size, and N_a is Avogadro's number, 6.0225×10^{26} kmol^{-1}. At this point the expanding gas reaches a velocity of, U_f, calculated as [*Wilson and Head*, 2017]:

$$0.5\, U_f^2 = 0.5\, U_v^2 + \frac{n_{gas}\, Q_u\, T_m}{m} \ln\frac{P_{ch}}{P_f} + \frac{1 - n_{gas}}{\rho_l}\left[P_{ch} - P_f\right] \quad (7)$$

The terminal velocity, u_t, by which the pyroclasts lags behind the expanding gas due to drag is calculated as [*Wilson et al.*, 2010]:

$$u_t = \left(\frac{4\, d\, \rho_c\, g}{3\, C_d\, \rho_g}\right)^{0.5} \quad (8)$$

where the Reynolds number is assumed to be large enough to be turbulent. Therefore, the initial ballistic velocity of each bead, U_b, can be calculated as:

$$U_b = U_f - u_t \quad (9)$$

From this point, the pyroclasts experience uninterrupted ballistic trajectory until deposition. Under conditions that may allow for an opaque gas cloud to form at the vent and thermally insulate the pyroclast, we compute the extent of that opaque cloud, *X*, from the maximum range of the pyroclasts following the treatment of *Wilson and Keil* [2012] for a fissure-like vent:

$$X = R_f - \frac{6.17\, \bar{d}\, {R_f}^{2.5}}{F_e} \quad (10)$$

The fissure-like geometry is assumed here to most closely reflect the shape of the inferred vents of the DMDs investigated in this study (**figure 1**). From the extent of the opaque gas cloud, the time each pyroclasts spent in the hot gas cloud, t_{cloud}, can be calculated and added to the time each pyroclast spends traveling in the dike post-fragmentation, t_{dike}, to compute the total time that each pyroclast spends above the closing temperature and experiences volatile loss by diffusion

$$t_{total} = t_{dike} + t_{cloud} \quad (11)$$

2.2 Diffusion model

To determine the fraction of water remaining in each pyroclast after being deposited, we solve for the diffusion of water in a sphere with radiation at the surface according to the diffusion equation [*Crank*, 1975]:

$$\frac{\partial C}{\partial t} = \frac{D(T)}{r^2}\frac{\partial}{\partial r}\left(r^2\frac{\partial C}{\partial r}\right) \quad (12)$$

$$\frac{\partial C}{\partial r}\Big|_{r=R} = \frac{-\beta}{D(T)}(C - C_o) \quad (13)$$

using an implicit, centered-space, finite-difference approximation. Further details of the discretization can be found in the supplementary text. The inputs to this diffusion model are the total time of diffusion, t_{total}, the size of the pyroclast, d, the evaporation rate β, and the rate of cooling [*Crank*, 1975]. The time for diffusion and the pyroclast size are determined from the eruption model through Eq. (2) and Eq. (10), while the evaporation rate and cooling rate remain unconstrained. We expand upon the work of *Saal et al.* [2008] to constrain these parameters by finding the range of evaporation and cooling rates that give satisfactory fits to the core to rim volatile profiles of H_2O, F, Cl, and S measured in several lunar pyroclastic glass beads. These calculations are made simultaneously for all four species and we use a Markov Chain Monte-Carlo approach to find the optimal set of evaporation and cooling rates that satisfy these profiles (see Supplements). The diffusion coefficients and activation energies used in the inversion are reported in *Watson and Bender* [1980] for Cl, *Zhang and Stolper* [1991] for H_2O, and *Dingwell and Scarfe* [1984] for F. For S, we use the assumption made in *Saal et al.* [2008] that the sulfur partitions primarily as S^2 at low f_{O2} [*Baker and Rutherford*, 1996] and that the activation energy should be similar to that of O^{2-} reported in *Wendlandt* [1991]. Finally, the diffusion coefficient for S is taken to be that reported in *Saal et al.* [2008].

With these calculations, we can determine the upper and lower bounds of percent water loss: an upper limit using the highest H_2O evaporation rate and lowest cooling rate that provide satisfactory fits, and a lower bound by using the lowest H_2O evaporation rate and highest cooling rate that provided satisfactory fits. It is not entirely clear how formation and emplacement processes of the green picritic glasses, from which the diffusion constraints are obtained, relate to inferred pyroclasts at DMDs which we attempt to model. However, the DMDs are believed to be picritic as well, and the conditions for volatile diffusion and surface evaporation are presumed to be similar.

Combining the eruption model outputs with the volatile diffusion and loss model results, we then calculate values of water content and pyroclast size with distance from the vent of the two DMDs. The size and water content of pyroclasts distributed radially away from the vent can then be converted to ESPAT values in two steps. First, we can calculate the particle size effect on ESPAT with [*Li and Milliken*, 2017; *Ralph E Milliken and Mustard*, 2005; 2007b]):

$$slope = 0.6608 + 4.7067\ exp(-0.04352\ d) \quad (14)$$

where *slope* refers to the slope of the linear relationship between ESPAT values and water content, which varies with particle size (*d*). The ESPAT values are then calculated based on the water content from the eruption and diffusion model [*Li and Milliken*, 2016; 2017; *Ralph E Milliken and Li*, 2017; *Ralph E Milliken and Mustard*, 2007b]:

$$ESPAT = \frac{1}{slope}\ wt\ \%\ H_2O \quad (15)$$

This approach is, in effect, a forward model of the near-IR water absorption strength based on the absorption path length (particle size) and concentration of the absorbing species (water content). The modeled ESPAT values can then be compared with the actual ESPAT value profiles from the M3 data and the parameters in the eruption model that result in the best fit can be determined. A schematic summary of the eruption-diffusion model is provided below in **figure 2**.

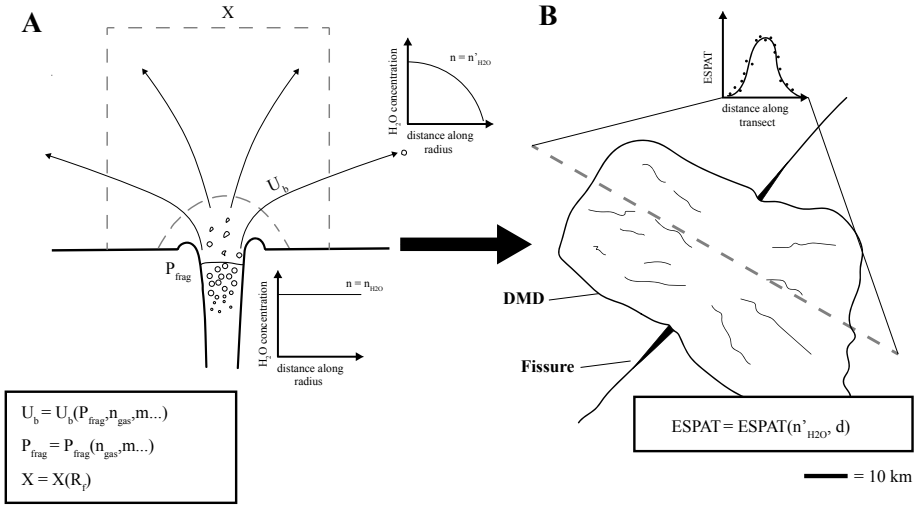

Figure 2. Schematic rendering of the eruption-diffusion model. **A** Schematic of critical stages of eruption model and how they depend on model parameters. **B** Schematic of resulting numerical ESPAT that results from the simulated eruption.

2.3 Markov chain Monte Carlo inversion

The section above describes the flow chart to run (forward) a realization of a synthetic ESPAT profile away from a vent. The next step is to develop a non-linear optimization scheme to find the free parameters, **m**

$$m = [n_{H_2O}, n_{gas}, \mu, \sigma] \quad (16)$$

that minimize the residual between the numerically simulated ESPAT profile and that of the measured DMD. The optimization is performed with a Markov chain Monte Carlo (MCMC) method. The MCMC is an inversion technique for non-linear problems and allows sampling of the posterior distribution of the model parameters of interest [*Anderson and Segall*, 2013]. The chain samples the posterior distribution by perturbing the model parameter vector **m** by a random amount in order to obtain **m**'. In this way, the future state of the chain obeys a Markovian process and depends only on the present state of the process when using the MCMC [*Anderson and Segall*, 2013]. From **m**', the forward eruption and water loss models are run and the ESPAT of the resulting deposit is calculated. If the residual is lowered between successive iterations, the new model parameters **m**' are saved and replace **m** for the next iteration. If the *residual* (L2-norm of the difference between observed and modeled ESPAT profiles) is not lowered, we compute the difference in likelihood between the solutions of the 2 consecutive iterations and use it to calculate the probability that the parameters of the last iteration are accepted. This finite probability allows a candidate vector, **m**', that may fail to lower the residual to still be accepted and allow the model to escape local extrema [*Anderson and Segall*, 2013]. This sequence is

repeated for *N* iterations until the posterior distribution has been adequately sampled (in this study *N*~20,000-40,000 iterations are sufficient to draw good statistics from the posteriori distributions).

3. Results

In order to obtain the upper and lower bounds of each parameter of the coupled eruption-water diffusion model, we explore the following scenarios: pyroclast diffusion calculations with boundary conditions that enhance water loss (corresponding to an evaporation rate of 3.5×10^{-5} m/s and a cooling rate of 0.1 ºC/s), as well as boundary conditions that limit water loss (corresponding to an evaporation rate of 1.4×10^{-6} m/s and a cooling rate of 6.4 ºC/s). These bounds are obtained from fitting diffusion profiles in the Apollo 15 green glasses measured by *Saal et al.* [2008]. Intermediate combinations of these boundary conditions are also explored and tabulated in **table 2**. The two DMDs investigated are Grimaldi, for which two ESPAT transects were evaluated (Grimaldi I and Grimaldi II), and Birt E. The measured ESPAT profiles for Grimaldi II are left unaltered, but some of the ESPAT values measured in the transects Grimaldi I and Birt E are not taken into account when calculating the misfit during the MCMC. Further details and justification about this omission can be found in the Discussion section. The modeled ESPAT profiles agree closely with ESPAT transects of the two DMDs (**figure 3, 5**). Parameters converged upon by the MCMC are summarized in **table 2**. Trace and covariate plots for different MCMC runs suggest convergence, with a burn-in period of ~1000-2000 iterations, depending on the initial seeds of the Markov chain **figure 4**.

DMD	n_{gas} (ppm)	n_{H2O} (ppm)	σ (phi)	μ (Φ)/d_{50} (μm)	n_{gas} (ppm)	n_{H2O} (ppm)	σ (phi)	μ (phi)	Evaporation rate (m/s)	Cooling rate (ºC/s)
Grimaldi II	9932 +/- 308	412 +/- 18	0.46	0.76/410	9800	400	0.49	0.74	1.4×10^{-6}	6.4
Grimaldi II	15,025 +/- 1,213	674 +/- 103	0.35	0.36/626	16,282	621	0.3	0.15	3.5×10^{-5}	6.4
Grimaldi II	9,745 +/- 614	400 +/- 16	0.55	0.71/372	5,000	100	1	1	1.4×10^{-6}	6.4
Grimaldi II	13,342 +/- 1,154	585 +/- 50	0.34	0.47/575	14,098	560	0.34	0.39	3.5×10^{-5}	0.1
Grimaldi II	14,314 +/- 1,322	773 +/- 135	0.38	0.46/573	15,342	704	0.34	0.33	1.4×10^{-6}	0.1
Grimaldi II	6,696 +/- 395	246 +/- 16	0.81	0.31/306	5,000	100	1	1	1.4×10^{-6}	6.4
Grimaldi II	7,290 +/- 224	266 +/- 10	1.06	-1.10/ 310	6,913	252	0.8	0.02	1.4×10^{-6}	0.1
Grimaldi II	12,612 +/- 1,264	507 +/- 53	0.38	0.48/565	12,267	512	0.41	0.56	3.5×10^{-5}	6.4
Grimaldi II	13,032 +/- 887	580 +/- 37	0.40	0.5/530	11,612	573	0.63	0.67	3.5×10^{-5}	0.1
Grimaldi I	29,038 +/- 1,788	805 +/- 152	0.79	-1.87/ 1,439	21,465	1,159	0.9	-2.08	1.4×10^{-6}	0.1
Grimaldi I	52,304 +/- 1,896	1317 +/- 244	0.20	-1.04/ 1,865	21,465	1,159	0.9	-2.08	3.5×10^{-5}	0.1
Grimaldi I	11,167 +/- 789	681 +/- 63	1.03	-1.29/ 545	11,310	634	0.9	-0.78	1.4×10^{-6}	6.4
Grimaldi I	21,480 +/- 1,535	1151 +/- 127	0.96	-2.1/ 1,058	21,465	1,159	0.9	-2.08	3.5×10^{-5}	6.4
Grimaldi I	7,226 +/- 3,3,938	497 +/- 118	1.12	-1.5/ 473	7,207	470	1.06	-0.92	1.4×10^{-6}	0.1
Grimaldi I	23,291 +/- 1,774	1138 +/- 576	0.8	-1.6/ 1,179	21,465	1,159	0.9	-2.08	3.5×10^{-5}	0.1
Grimaldi I	6,891 +/- 409	474 +/- 35	1.13	-1.59/ 1,495	7,106	481	0.96	-0.98	1.4×10^{-6}	6.4

Grimaldi I	19,490 +/- 983	1055 +/- 103	0.92	-2.09/ 1,265	21,465	1,159	0.9	-2.08	3.5×10^{-5}	6.4
Birt E	5,490 +/- 856	505 +/- 58	0.62	0.34/1,265	4,397	522	0.76	0.78	1.4×10^{-6}	0.1
Birt E	6998 +/- 58	910 +/- 48	1.77	-2.33/53	4,397	522	0.76	0.78	3.5×10^{-5}	0.1
Birt E	4,642 +/- 371	459 +/- 54	0.47	1.26/291	4,397	522	0.76	0.78	1.4×10^{-6}	6.4
Birt E	12,076 +/- 1,317	962 +/- 197	0.18	0.36/713	4,397	522	0.76	0.78	3.5×10^{-5}	6.4
Birt E	4,649 +/- 256	420 +/- 47	0.72	0.38/363	4,172	468	0.78	0.61	1.4×10^{-6}	0.1
Birt E	6,959 +/- 400	982 +/- 102	0.82	0.96/195	8,000	911	0.69	0.65	3.5×10^{-5}	6.4
Birt E	4,776 +/- 552	448 +/- 51	0.69	0.45/356	4,397	422	0.76	0.78	1.4×10^{-6}	6.4
Birt E	7,168 +/- 454	1188 +/- 143	0.76	0.93/214	4,397	522	0.76	0.78	3.5×10^{-5}	0.1

Table 2. Table summarizing all of the MCMC runs performed in this study. Runs in light blue indicate simulations with out a thermally opaque gas cloud. Parameters highlighted in grey indicate initial starting values for each MCMC while parameters to the left of the highlighted region indicate the parameters that result in the best fit for each run.

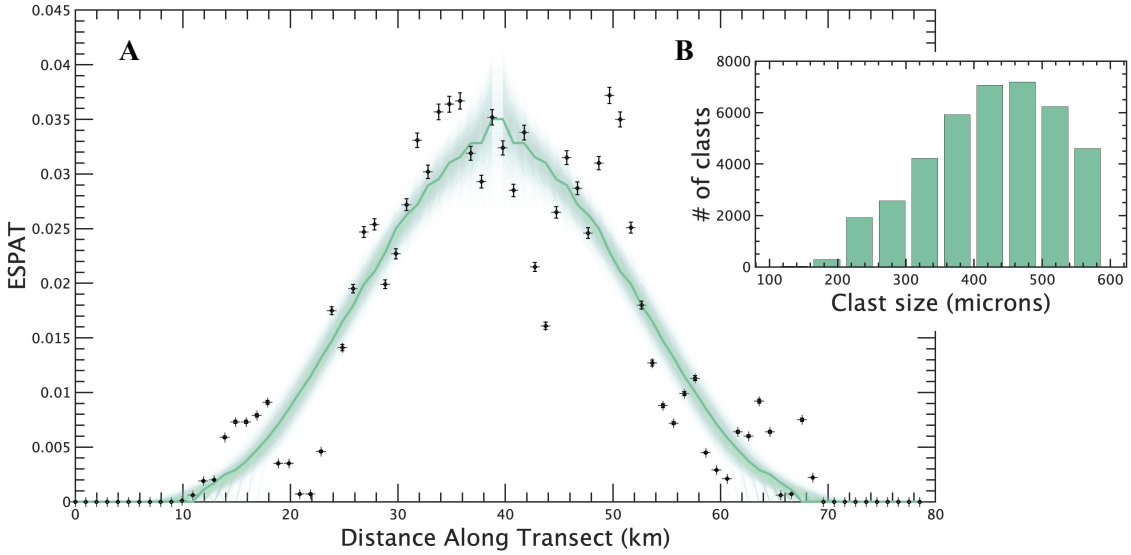

Figure 3. A The solid line represents the best fitting model for the second transect for the DMD Grimaldi II for an MCMC run of 10,000 iterations and an evaporation rate of 1.4×10^{-6} m/s and a cooling rate of 6.4 ºC/s. The green shaded area brackets the resulting ESPAT profiles sampled after the burn-in period (~1000 iterations). **B** The resulting pyroclast size distribution for the best fitting model.

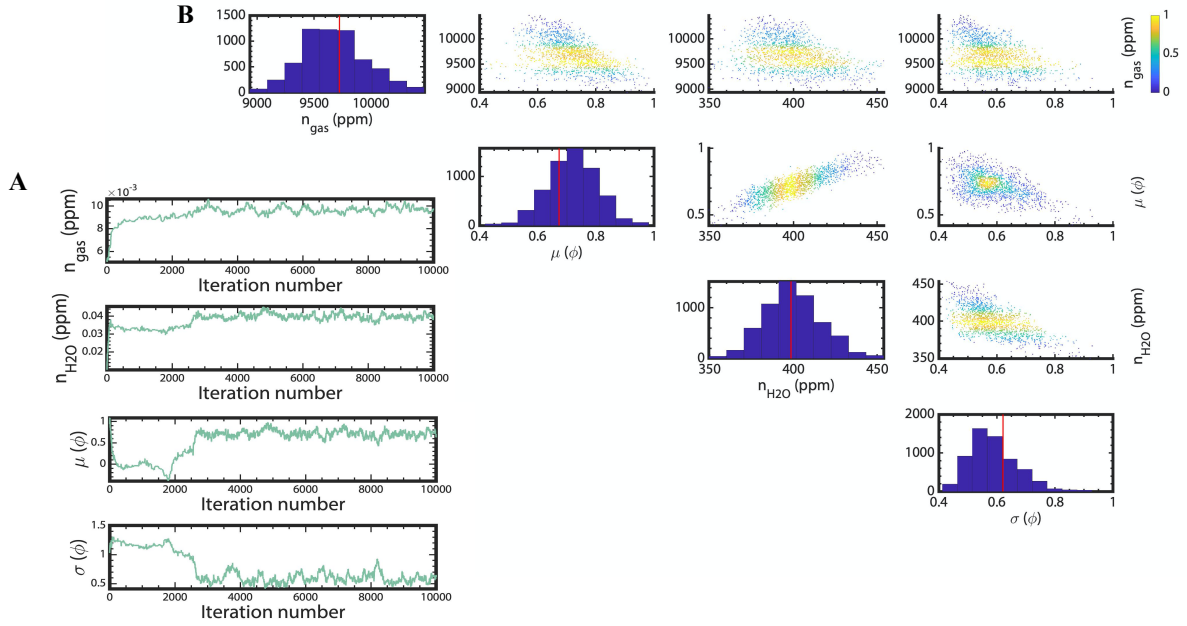

Figure 4. A Trace plots for MCMC run on Grimaldi II with an evaporation rate of 1.4 x 10^{-6} m/s and a cooling rate of 6.4 ºC/s. **B** Along diagonal of matrix of plots is the marginal posteriori distribution for each parameter with the solid red line representing the most likely solution in the parameter space, while the off-diagonal scatter plots highlight the covariance between parameters sampled from the posteriori distribution after burn-in.

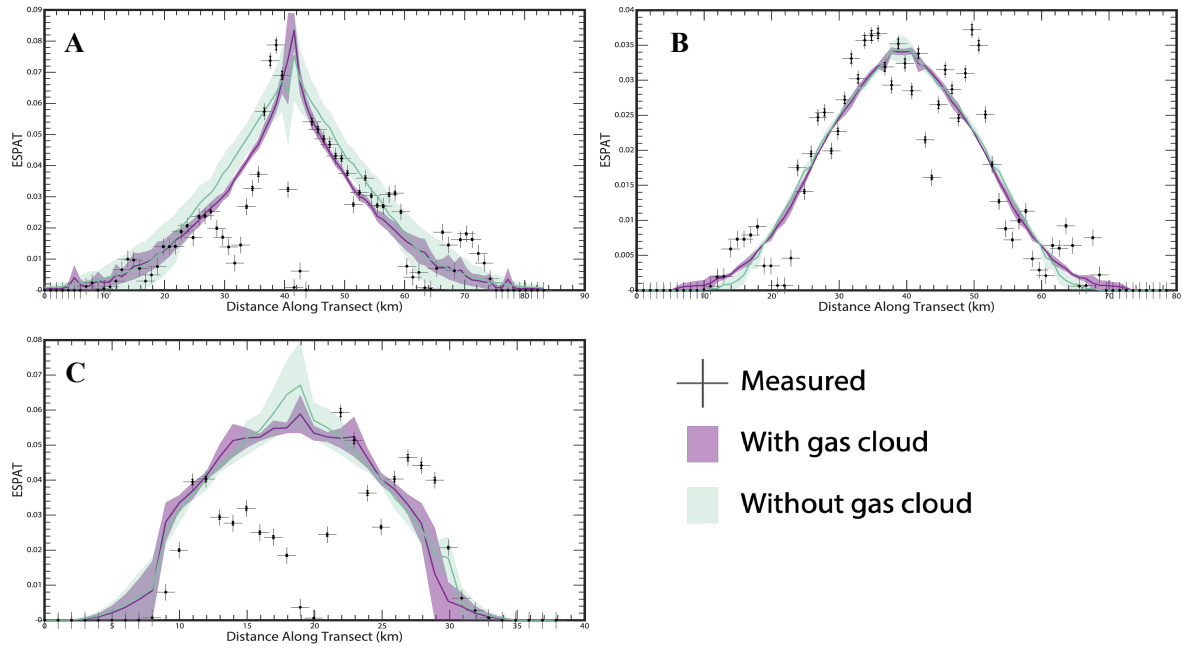

Figure 5. Best fitting models to the measured ESPAT profile for each combination of evaporation rate and cooling rate for **A** Grimaldi I, **B** Grimaldi II, and **C** Birt E. The solid line indicates the most likely solution, light shades indicate total range spanned by the posteriori distribution of the MCMC for inversions that include and neglect the presence of an opaque gas cloud.

3.2 n_{H2O}

Across all best fitting models for all of the DMDs, modeled with and without a thermally opaque gas cloud, best-fitting models retrieve n_{H2O} values that exhibit a total range from 246 +/- 16 ppm to 1,317 +/- 244 ppm. The error bounds are calculated as the standard deviation of the parameter's posteriori distribution sampled by the MCMC across the entire simulation after burn-in.

The best-fit solutions for Grimaldi I correspond to n_{H2O} values that range from 681 +/- 63 ppm to 1317 +/- 244 ppm when accounting for a thermally opaque gas cloud during the eruption compared to the range from 474 +/- 35 ppm to 1138 +/- 576 ppm in the absence of a thermally opaque gas cloud. The lower and upper bound values for both cases are obtained with the least and most efficient water loss diffusion scenarios respectively. Comparatively, the n_{H2O} values of best-fitting models for Grimaldi II return ranges from 400 +/- 16 ppm to 773 +/- 135 ppm (with gas cloud) and from 246 +/- 16 ppm to 580 +/- 37 ppm (without gas cloud). Finally, for Birt E, the best solution yields n_{H2O} values that range from 459 +/- 54 ppm to 962 +/- 197 ppm (with gas cloud) and from 420 +/- 47 ppm to 1188 +/- 143 ppm (without gas cloud). Additionally, for each DMD, we see that the returned pre-fragmentation concentrations of water, n_{H2O}, consistently increase as evaporation rate increases and cooling rate decreases **table 2**. For all of the DMDs, all else equal, the presence of a thermally opaque gas cloud results in higher pre-fragmentation water content (n_{H2O} values).

3.3 n_{gas}

Best-fitting models for all of the DMDs, both with and without a thermally opaque gas cloud, return corresponding n_{gas} values that exhibit a range from 4,642 +/- 371 ppm to 52,304 +/- 1,896 ppm. The range of n_{gas} values for each individual DMD both with and without a thermally opaque gas cloud can be found in **table 2**.

For each DMD, we see that the returned exsolved gas concentration upon fragmentation, n_{gas}, are also positively correlated with the inferred evaporation rate and negatively correlated with the cooling rate **table 2**. For the range of n_{gas} values returned, the corresponding confining pressure at the level of fragmentation range from ~1 – 11 MPa. The lower end of this range corresponds to models run for the less extensive Birt E deposit (~39 km transect) considering low evaporation rates and high cooling rates, whereas the higher end corresponds to the longer Grimaldi I transect (~85 km) and an assumption of high evaporation rates and low cooling rates **table 2**. In all cases modeled, except for Birt E with an evaporation rate of 1.4×10^{-6} m/s and a cooling rate of 6.4 ºC/s, the presence of a thermally opaque gas cloud implies lower n_{gas} values (**table 2)**.

3.4 Pyroclast size distribution μ and σ

For convenience, pyroclast size distribution is discussed in terms of the best-fitting models of pyroclast size in units of micrometers that corresponds to the 50th percentile of the size distribution, d_{50}. Across all best fitting models for all of the DMDs, modeled with and without a thermally opaque gas cloud, d_{50} ranges from 53 to 1,865 μm. The range of d_{50} values for each individual DMD both with and without a thermally opaque gas cloud can be found in **table 2**. For each DMD, with few exceptions, the pyroclast size corresponding to the 50th percentile is positively correlated to evaporation rate and negatively correlated to cooling rate.

4. Discussion

Of the three DMD transects that were modeled, Grimaldi II exhibits a complete, continuous, and symmetric spatial ESPAT distribution, and thus offers the most robust constraints for the eruption-diffusion model (**figure 1**). Asymmetry in the ESPAT maps and profiles (**figure 1, 5**) can be explained in several ways, including an angled conduit at the lunar surface, non-uniform topography, and uneven weathering or overlap of a younger unit. Additionally, Grimaldi I and Birt E both have ESPAT values of zero at the inferred vent, which is where one would expect ESPAT values to be highest as the largest pyroclasts are deposited near the vent and retain more water. Lower ESPAT values at or near the vent could possibly be explained by significant water loss for particles remaining within a thermally opaque cloud throughout the transport and perhaps even shortly after deposition. Alternatively, M3 pixels (spectra) directly over and adjacent to the vents can have low signal due to shadowing effects (e.g., see shadows for Birt E in Figure 1), which can result in falsely low values. Small-scale shadowing effects due to small impact craters and impact excavation of anhydrous material that lies beneath the DMD material may also explain some of the pixel-to-pixel variability in ESPAT values along the transects, such as some of the low points observed in Figure 5A for Grimaldi I. For simplicity, we omit these anomalous data points towards the center of the Grimaldi I and Birt E transects and focus instead on the tails of the ESPAT distribution away from the vent as they are more sensitive to eruption dynamics and pyroclast size distribution. Despite this omission, the range of values returned for each parameter for the three modeled ESPAT transects show significant overlap. To our knowledge, these results offer tighter constraints on these parameters for lunar pyroclastic eruptions and associated magma source regions than previously offered [*Hauri et al.*, 2011; *Rutherford et al.*, 2017; *Saal et al.*, 2008; *Saal et al.*, 2013]. Importantly, the results also demonstrate that reasonable values for these parameters can be achieved that both fit the remotely sensed near-IR data and are consistent with current pyroclastic eruption models.

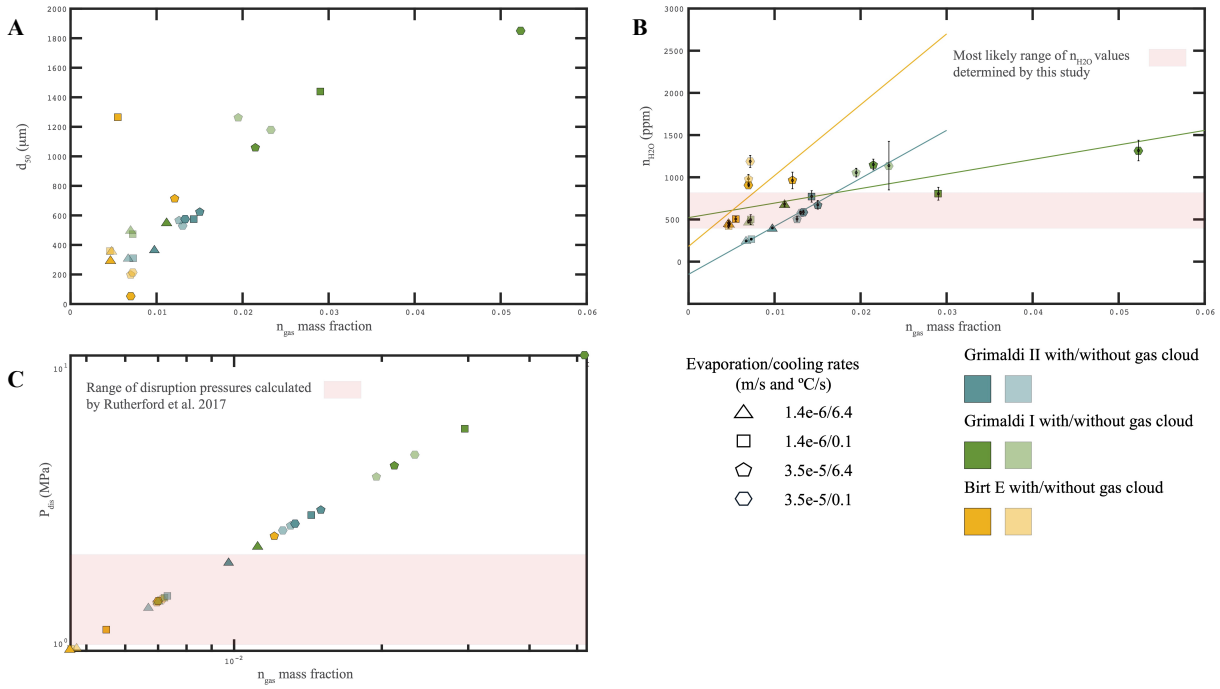

Figure 6. The parameters that resulted in the best fitting models for each MCMC run are plotted here. **A** Pyroclast size corresponding to the 50th percentile, **B** wt % H_2O pre-fragmentation, and **C** fragmentation pressure vs mass

fraction of exsolved gas at fragmentation. The range highlighted in panel **C** corresponds to the range of fragmentation depths for the orange picritic glasses determined petrologically by [*Rutherford et al.*, 2017].

4.1 n_{H2O}

For a given ESPAT transect, as one considers a scenario that would enhance water loss (slower cooling rate or higher evaporation rate), the best fit model parameters are adjusted by increasing the amount of pre-fragmentation water such that the quality of the ESPAT profile fit is maintained (**table 2**). A satisfactory fit can be found for each combination of evaporation and cooling rate applied to each transect, but the only overlap in solution space in terms of pre-fragmentation water content between all three DMD transects occurs in a narrow range from ~400 – 800 ppm **figure 6**.

For Grimaldi, considering both transects, the range for pre-fragmentation water content likely ranges from ~400 – 800 ppm on the basis of the overlap in n_{H2O} solution space both with and without gas cloud, or ~500 – 600 ppm if considering only the scenarios without a thermally opaque gas cloud (**table 2**; **figure 6**). Because Grimaldi I and II were transects measured across the same DMD, the true pre-fragmentation water returned by the eruption-diffusion model should agree. Assuming the presence of a thermally opaque gas cloud, the only models for both Grimaldi I and II that fall within this overlapping solution space are the scenario with an evaporation rate of 1.4 x 10^{-6} m/s and 6.4 ºC/s (**figure 6**; **table 2**). For models without a thermally opaque gas cloud, no combination of evaporation rate and cooling rate returns n_{H2O} values that fall within a common range for both Grimaldi I and II (**figure 6, table 2**). This may suggest the presence of a thermally opaque gas cloud at Grimaldi.

For Birt E, the best fitting models for the same evaporation rate of 1.4 x 10^{-6} m/s and cooling rates of either 0.1 and 6.4 ºC/s also return pre-fragmentation water concentrations consistent with that of Grimaldi, 400 – 800 ppm (**figure 6**; **table 2**), while n_{H2O} values for best fitting models with an evaporation rate of 3.5 x 10^{-5} m/s and either a cooling rate of 0.1 or 6.4 ºC/s yield higher values from 910 to 1188 ppm. While the n_{H2O} values returned for Birt E that were obtained assuming high evaporation rates could be explained by the presence of spatial heterogeneities in the distribution of water in DMD source material, the values for n_{H2O} remain within the range modeled for Grimaldi I (**figure 6**; **table 2**). Because of this, it is likely that the pre-fragmentation water content in these DMD source materials is similar and that the evaporation rate during lunar eruptions tends towards values closer to that of 1.4 x 10^{-6} m/s, at least for eruptions with a thermally opaque gas cloud.

The most likely range of water contents determined in this study (400 – 800 ppm) is in good agreement with the most likely range of water contents previous studies have reported for parts of the lunar interior sampled by the lunar picritic glasses (260 – 745 ppm; *Saal et al.* [2008], 615 – 1410 ppm; *Hauri et al.* [2011]). Our results support the growing body of work that suggests parts of lunar interior are more enriched in volatiles than previously thought [*Hauri et al.*, 2011; *Rutherford et al.*, 2017; *Saal et al.*, 2008; *Saal et al.*, 2013]. Source magma water content inferred from the ESPAT values calculated for the DMDs studied here suggest a maximum range of 246 – 1317 ppm (**figure 6**; **table 2**). These values are a lower bound as they don't take into account any water lost from outgassing pre-fragmentation. We note however, that the data from olivine melt inclusions in Apollo 17 orange glass beads suggest a very small H_2O fraction in the pre-fragmentation gas phase. Additionally, these values may not be representative of the bulk

lunar mantle as the lunar glasses are believed to be generated from partial melting of differentiated and likely volatile enriched LMO material [*J W Delano*, 1986; *Hess and Parmentier*, 1995; *C K Shearer et al.*, 2006], and the degree of partial melting is estimated to be 5-10% [*Saal et al.*, 2008].

4.2 n_{gas}

The exsolved gas concentration upon fragmentation, n_{gas}, exerts important controls over the model and, ultimately, the fit to the observed ESPAT data. The value of n_{gas} directly influences the depth of fragmentation, the size of the thermally opaque gas cloud (if any), the trajectories of the pyroclasts forming the deposit, and consequently the extent of water loss by degassing. As water loss is enhanced, the values of n_{gas} that result in the closest ESPAT fits tend to increase (**table 2**). This is largely because at a fixed n_{gas}, the distribution of pyroclasts away from the vent remains identical but enhanced water loss decreases the calculated ESPAT values across the profile. To counteract this effect and retrieve an acceptable fit to observed ESPAT profiles, the solution space is shifted towards a larger pyroclast size distribution (i.e., if the concentration of the absorbing species decreases then the absorption path length must increase to maintain the same absorption strength). To enable the larger pyroclasts to travel the same distance, the n_{gas} must increase so that the pyroclasts inherit enough kinetic energy to match the extent of the observed water signature in the near-IR data.

For the range of n_{gas} values returned, the corresponding pressure at the fragmentation level ranges from ~1 – 11 MPa (**figure 6**). Considering the Grimaldi models with overlapping solution space as well as all of the best fitting models for Birt E, this range reduces to ~1-3 MPa (**figure 6**; **table 2**). This lower range is in close agreement with values determined from petrological studies using C dissolved in melt inclusions in picritic orange glasses that suggest fragmentation at ~1-2 MPa [*Rutherford et al.*, 2017]. We reiterate that the composition of the exsolved gas at fragmentation used for the models is that reported by *Rutherford et al.* [2017], with a molar mass of 36 g/mol. To investigate the dependence of our results on the composition of the exsolved gas, for the least efficient water loss conditions applied to Grimaldi II, two additional MCMCs were run: one with an arbitrary molar mass of exsolved gas of 20 g/mol and with 65 g/mol. Assuming a molar mass for the gas mixture of 65 g/mol, we find that the disruption pressure is decreased by less than 0.1 MPa and the pre-fragmentation water content reduced from 400 to 340 ppm. Using instead 20 g/mol, the disruption pressure is increased by ~0.5 MPa and the pre-fragmentation water content is increased from 400 to 520 ppm. This range in possible molar masses for a given composition of exsolved gas represents extreme upper and lower bounds and seems to suggest that the composition does not significantly alter the results.

As determined by *Rutherford et al.* [2017] based on gas solubility experiments and analyses of the orange picritic glasses, the abundance of exsolved gas at the transition from equilibrium to kinetic degassing is too low to lead to magma fragmentation. Using C values measured in the orange picritic glass, *Rutherford et al.* [2017] estimate the depth of fragmentation to be within 300 – 600 m from the surface (1-2 MPa), and therefore determine that there is a contribution from open system degassing. The concentration of exsolved volatiles at fragmentation returned by our models are in excess of those calculated by *Rutherford et al.* [2017] for closed system degassing. The difference between the values of n_{gas} returned by our model and the closed-system degassing calculated by *Rutherford et al.* [2017] (~200 ppm) represents the contributions

from open-system degassing. The inability of closed-system degassing to cause fragmentation at depths that agree with those determined petrologically by *Rutherford et al.* [2017] in the orange picritic glasses as well as the large n_{gas} values determined in this study can at least in part be explained by the dike-tip propagation model of lunar glass formation proposed by *Head and Wilson* [2017]. In this model, efficient open system degassing allows a volatile-rich foam to form at the tip of a propagating dike and propels the orange picritic glass magma to the lunar surface.

4.3 Pyroclast size distribution μ and σ

The pyroclast size distribution affects the ballistic trajectory of the pyroclast, the loss of volatiles by diffusion, and also directly influences the modeled ESPAT values. This effect of pyroclast size on water loss can be seen as models trade-off between pyroclast size and the assumed conditions for water loss (evaporation and cooling rates). Models run under conditions that do not favor volatile retention (high evaporation rates and low cooling rates) return larger average pyroclast size distributions because larger pyroclasts retain water more readily than smaller pyroclasts (**figure 6**; **table 2**). Furthermore, the lateral extent of the modeled deposits depends on the pyroclast size distribution because smaller pyroclasts inherit a greater proportion of the momentum of the expanding gas cloud, which explains the positive correlation between average pyroclast size and mass fraction exsolved gas at fragmentation.

Across all of the best models, the returned pyroclast size distributions are such that d_{50} ranges from 53 to 1,865 μm (**figure 6**; **table 2**). When considering the added constraints for the fragmentation depth from *Rutherford et al.* [2017], this range reduces to 53 to 1,265 μm (**figure 6**). For Grimaldi, when considering only the models with parameters that overlap for Grimaldi I and II, the range in pyroclast sizes is further reduced to 372 - 626 μm (**figure 6**; **table 2**). For Birt E, the total range in pyroclast sizes (again 50th percentile) range from 53 to 1,265 μm for the best fitting models (**figure 6**; **table 2**). Despite the large range in pyroclast sizes determined by the inversion calculation, the solutions with the highest likelihood agree with the observation that the picritic glasses are submillimeter (<1 mm) [*G H Heiken et al.*, 1991; *Rutherford et al.*, 2017; *Saal et al.*, 2008].

4.3 Constraints on evaporation and cooling rate

In addition to each of the parameters constrained by this work, we find that the combinations of evaporation rate and cooling rate that provide mutual satisfactory fits to the two Grimaldi transects only occur at low evaporation rates (10^{-6} m/s) (**figure 6**; **table 2**), in agreement with the low evaporation rates determined experimentally by *Arndt et al.* [1984], and with the diffusion profiles modeled numerically by *Saal et al.* [2008]. However, we find that only cooling rates slightly above the range determined by *Saal et al.* [2008] (<5ºC/s) provide model results that agree between the two Grimaldi transects (6.4 Cº/s) (**figure 6**; **table 2**) for models with a gas cloud. In fact, for Grimaldi I, for either evaporation rate of 1.4 x 10^{-6} or 3.5 x 10^{-5} m/s, with a cooling rate of 0.1 ºC/s, a satisfactory fit with ESPAT data cannot be provided when accounting for a thermally opaque gas cloud. This is because under these enhanced water loss conditions the average pyroclast size corresponding to best fitting models needs to be large in order to limit water loss, and consequently (**table 1**) the size of the thermally opaque gas cloud vanishes in Eq. (9). ESPAT values for the Birt E transect, however, can be adequately fit using any combination of evaporation rate (either 1.4 x 10^{-6} m/s or 3.5 x 10^{-5} m/s) and cooling rate (0.1 or 6.4 ºC/s). Moreover, all combinations for the water loss for Birt E provide reasonable fits within the

fragmentation depth constraints of *Rutherford et al.* [2017] (fractionation depths of 300 – 500 m) (**figure 6**; **table 2**).

4.5 Agreement of n_{H2O} and pyroclast size distribution with previous observations

The DMDs investigated in the present study are not related to the sites from which samples were returned by the Apollo and Luna missions. The returned picritic glass samples display a typical range of mean pyroclast size of 45 -100 μm [*G H Heiken et al.*, 1991; *Rutherford et al.*, 2017]. For the most probable best-fitting models, those that agree with the fragmentation depth determined by *Rutherford et al.* [2017] as well as the models that provide agreement between the two ESPAT transects for Grimaldi, the pyroclast size corresponding to 50th percentile range from 372 to 1,265 μm. This is larger than the range of average pyroclast sizes observed in the Apollo soils [*G H Heiken et al.*, 1991]. The discrepancy can be attributed, at least in part, to the fact that samples at or near a known vent have not been acquired. Samples from this region would contain larger pyroclasts and potentially be less well-sorted.

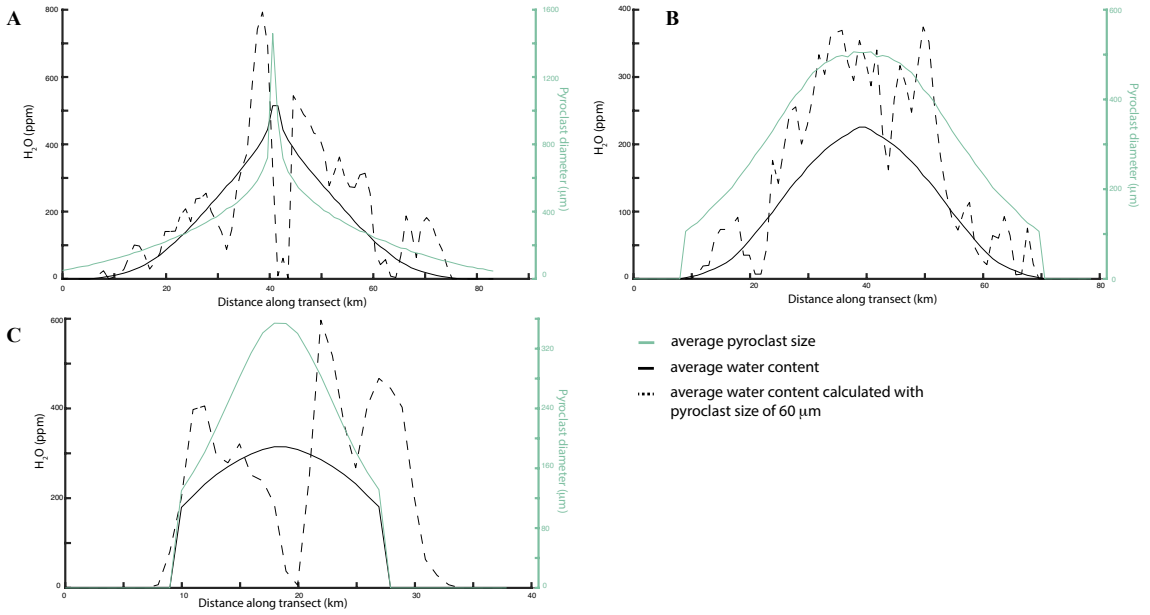

Figure 7. Average pyroclast diameter determined and post-deposition water content from best-fitting models for **A** Grimaldi I, **B** Grimaldi II, and **C** Birt E, along with water contents calculated similar to those of Milliken and Li (2017) using fixed pyroclast diameter of 60 μm. Each of the best-fitting models here are for evaporation and cooling rates of 1.4 x 10^{-6} m/s and 6.4 ºC/s, respectively.

4.6 Agreement distribution of water in lunar pyroclastic deposits reported in Milliken and Li (2017)

The final distribution of water and average pyroclast diameter corresponding to each best-fitting simulation with water-loss calculated with evaporation and cooling rates of 1.4 x 10^{-6} m/s and 6.4 ºC/s, respectively, are reported in **figure 7**. *Ralph E Milliken and Li* [2017] assumed the DMDs investigated were spectrally dominated by particles (pyroclasts) ~60-80 μm in diameter in order to the amount of water indigenous to the deposits. The results presented in this study instead solve for pyroclast size and find that the pyroclast size distributions that result in the best-fitting models are on average larger than that used in *Ralph E Milliken and Li* [2017], sometimes

by an order of magnitude. This results in the current DMD water contents reported in *Ralph E Milliken and Li* [2017] to be, on average, higher than the results presented in this work. Despite the large differences in pyroclast sizes (**figure 7**), the differences in the final water contents of the DMDs is not huge and it is still clear that the DMDs are more hydrated than surrounding regions. Most importantly, the results described here demonstrate that there exist a suite of conditions for which the near-IR spectral data can be modeled and which are simultaneously consistent with current eruption models. The integration of the models and the remotely sensed data further support the notion that the magmas that gave rise to the DMDs are enriched in water.

5. Conclusion

Constraining the lunar volatile budget is important to further our understanding of lunar formation and evolution as well as volcanic eruptions. Models of lunar formation and evolution must be able to explain the retention of volatiles in parts of the lunar interior [*Hauri et al.*, 2011; *Rutherford et al.*, 2017; *Saal et al.*, 2008; *Saal et al.*, 2013]. The present study offers constraints on the pre-fragmentation water content of glass erupted and forming two Dark Mantle Deposits (DMDs) where we can use spectral data to extract information about water content and pyroclast size.

Our results suggest that the most likely range in water content in the glass before fragmentation is 400 – 800 ppm. The most probable range of pre-fragmentation water contents for the very-low Ti glasses is 260 – 745 ppm according to *Saal et al.* [2008] and 615 – 1410 ppm from *Hauri et al.* [2011]. Our results are in close agreement with that of *Saal et al.* [2008], which provided the data from which evaporation and cooling rate constraints were obtained, and is only slightly lower than the range determined by *Hauri et al.* [2011]. This is likely because *Hauri et al.* [2011] obtained the range in water content by analyzing dissolved water in melt inclusions, capturing the trend of decreasing H2O in trapped melt with decreasing pressure just prior to melt fragmentation. The method used in this study not only provides tighter constraints on pre-fragmentation water contents, but it also provides constraints for the concentration of exsolved gas at fragmentation and constraints for the pyroclast size distribution of DMDs. The concentration of exsolved volatiles at fragmentation according to our best-fitting models are in excess of the concentrations calculated by *Rutherford et al.* [2017] assuming closed system degassing. This supports their conclusion that open system degassing plays a significant role on the eruption dynamics of these fire fountain eruptions and is in part explained by the dike formation model of *Wilson and Head III* [2003] and *Head and Wilson* [2017].

The calculations for water loss use a range of evaporation and cooling rates obtained by fitting diffusion data for the very low-Ti lunar glasses. Therefore, an important assumption this model makes is that the diffusional environment for the pyroclasts associated with the DMDs being investigated is similar to the very low-Ti, green lunar glasses. Additionally, the constraints on fragmentation come from calculations made on the high-Ti, orange lunar glasses and may not be applicable to the DMDs investigated here. The orange glasses are believed to have a higher cooling rate than the other lunar glasses [*Arndt et al.*, 1984; *Arndt and Von Engelhardt*, 1987], and if indeed the DMDs investigated here more closely represent the orange glasses, the pre-fragmentation water content, the exsolved gas concentration at fragmentation, and the mean pyroclast size returned by the best fitting models would likely decrease (**figure 6**; **table 2**).

Additional information on the titanium content of lunar DMDs could further constrain the results presented here.

This study suggests that in the absence of new samples returned from the Moon, a combination of remote sensing, numerical modeling, and petrology can be used to determine the composition of the source material tapped by volcanic eruptions. The extent to which different parts of the lunar interior may exhibit heterogeneous amounts of volatiles may not be entirely determinable at present from the two DMDs investigated in this study, but the template presented here may help fill in those gaps.

6. Acknowledgements

We greatly thank M.J. Rutherford, J.W. Head, and E. First for their ideas and guidance on this project as well as their edits and reviews made on the manuscript. Codes are available and archived at the Brown Digital Repository, Brown University Library, https://doi.org/10.26300/8pmw-yw23.

References

Anderson, K., and P. Segall (2013), Bayesian inversion of data from effusive volcanic eruptions using physics-based models: Application to Mount St. Helens 2004–2008, *Journal of Geophysical Research: Solid Earth*, *118*(5), 2017-2037.

Arndt, J., W. Engelhardt, I. Gonzalez-Cabeza, and B. Meier (1984), Formation of Apollo 15 green glass beads, *Journal of Geophysical Research: Solid Earth*, *89*(S01), C225-C232.

Arndt, J., and W. Von Engelhardt (1987), Formation of Apollo 17 orange and black glass beads, *Journal of Geophysical Research: Solid Earth*, *92*(B4), E372-E376.

Asimow, P. D., Langmuir, and CH (2003), The importance of water to oceanic mantle melting regimes, *Nature*, *421*(6925), 815-820.

Atkinson, K. E. (1989), An introduction to numerical analysis*Rep.*

Baker, L., and M. J. Rutherford (1996), Sulfur diffusion in rhyolite melts, *Contributions to Mineralogy and Petrology*, *123*(4), 335-344.

Boyce, J. W., Y. Liu, G. R. Rossman, Y. Guan, J. M. Eiler, E. M. Stolper, and L. A. Taylor (2010), Lunar apatite with terrestrial volatile abundances, *Nature*, *466*(7305), 466-469.

Canup, R. M. (2004), Dynamics of lunar formation, *Annu. Rev. Astron. Astrophys.*, *42*, 441-475.

Crank, J. (1975), The Mathematics of Diffusion: Oxford University, *New York*, *19752*, 1-21.

Delano, J. (1980), Chemistry and liquidus phase relations of Apollo 15 red glass Implications for the deep lunar interior, paper presented at Lunar and Planetary Science Conference Proceedings.

Delano, J. (1990), Buoyancy-driven melt segregation in the earth's moon. I-Numerical results, paper presented at Lunar and Planetary Science Conference Proceedings.

Delano, J., and D. Lindsley (1983), Mare glasses from Apollo 17: Constraints on the Moon's bulk composition, *Journal of Geophysical Research: Solid Earth*, *88*(S01), B3-B16.

Delano, J. W. (1986), Pristine lunar glasses: Criteria, data, and implications, *Journal of Geophysical Research: Solid Earth*, *91*(B4), 201-213.

Dingwell, D. B., and C. M. Scarfe (1984), Chemical diffusion of fluorine in jadeite melt at high pressure, *Geochimica et Cosmochimica Acta*, *48*(12), 2517-2525.

Elkins, L., V. Fernandes, J. Delano, and T. Grove (2000), Origin of lunar ultramafic green glasses: Constraints from phase equilibrium studies, *Geochimica et Cosmochimica Acta*, *64*(13), 2339-2350.

745 Elkins-Tanton, L. T., N. Chatterjee, and T. L. Grove (2003), Experimental and petrological
746 constraints on lunar differentiation from the Apollo 15 green picritic glasses, *Meteoritics &*
747 *Planetary Science*, *38*(4), 515-527.
748 Fogel, R. A., and M. J. Rutherford (1995), Magmatic volatiles in primitive lunar glasses: I. FTIR
749 and EPMA analyses of Apollo 15 green and yellow glasses and revision of the volatile-assisted
750 fire-fountain theory, *Geochimica et Cosmochimica Acta*, *59*(1), 201-215.
751 Gaddis, L., C. Rosanova, T. Hare, B. Hawke, C. Coombs, and M. Robinson (1998), Small lunar
752 pyroclastic deposits: a new global perspective, *LPI*(1807), 1807.
753 Gaddis, L. R., B. R. Hawke, M. S. Robinson, and C. Coombs (2000), Compositional analyses of
754 small lunar pyroclastic deposits using Clementine multispectral data, *Journal of Geophysical*
755 *Research: Planets*, *105*(E2), 4245-4262.
756 Gaddis, L. R., C. M. Pieters, and B. R. Hawke (1985), Remote sensing of lunar pyroclastic
757 mantling deposits, *Icarus*, *61*(3), 461-489.
758 Gaddis, L. R., M. I. Staid, J. A. Tyburczy, B. R. Hawke, and N. E. Petro (2003), Compositional
759 analyses of lunar pyroclastic deposits, *Icarus*, *161*(2), 262-280.
760 Gaetani, G. A., and T. L. Grove (1998), The influence of water on melting of mantle peridotite,
761 *Contributions to Mineralogy and Petrology*, *131*(4), 323-346.
762 Greenwood, J. P., S. Itoh, N. Sakamoto, P. Warren, L. Taylor, and H. Yurimoto (2011),
763 Hydrogen isotope ratios in lunar rocks indicate delivery of cometary water to the Moon, *Nature*
764 *Geoscience*, *4*(2), 79-82.
765 Gustafson, J. O., J. F. Bell, L. R. Gaddis, B. R. Hawke, and T. A. Giguere (2012),
766 Characterization of previously unidentified lunar pyroclastic deposits using Lunar
767 Reconnaissance Orbiter Camera data, *Journal of Geophysical Research: Planets*, *117*(E12).
768 Hapke, B. W., R. M. Nelson, and W. D. Smythe (1993), The opposition effect of the moon: the
769 contribution of coherent backscatter, *Science*, *260*(5107), 509-511.
770 Hauri, E. H., T. Weinreich, A. E. Saal, M. C. Rutherford, and J. A. Van Orman (2011), High pre-
771 eruptive water contents preserved in lunar melt inclusions, *Science*, *333*(6039), 213-215.
772 Head, J. W. (1974), Lunar dark-mantle deposits-possible clues to the distribution of early mare
773 deposits, paper presented at Lunar and Planetary Science Conference Proceedings.
774 Head, J. W., and L. Wilson (2017), Generation, ascent and eruption of magma on the Moon:
775 New insights into source depths, magma supply, intrusions and effusive/explosive eruptions
776 (Part 2: Predicted emplacement processes and observations), *Icarus*, *283*, 176-223.
777 Heiken, G., and D. McKay (1977), Model for eruption behavior of a volcanic vent in Eastern
778 Mare Serenitatis*Rep.*, Los Alamos Scientific Lab., NM (USA).
779 Heiken, G. H., D. T. Vaniman, and B. M. French (1991), Lunar sourcebook-A user's guide to the
780 moon, *Research supported by NASA,. Cambridge, England, Cambridge University Press, 1991,*
781 *753 p. No individual items are abstracted in this volume.*
782 Hess, P. C., and E. Parmentier (1995), A model for the thermal and chemical evolution of the
783 Moon's interior: Implications for the onset of mare volcanism, *Earth and Planetary Science*
784 *Letters*, *134*(3-4), 501-514.
785 Hirth, G., and D. L. Kohlstedt (1996), Water in the oceanic upper mantle: implications for
786 rheology, melt extraction and the evolution of the lithosphere, *Earth and Planetary Science*
787 *Letters*, *144*(1-2), 93-108.
788 Hui, H., Y. Guan, Y. Chen, A. H. Peslier, Y. Zhang, Y. Liu, R. L. Flemming, G. R. Rossman, J.
789 M. Eiler, and C. R. Neal (2017), A heterogeneous lunar interior for hydrogen isotopes as
790 revealed by the lunar highlands samples, *Earth and Planetary Science Letters*, *473*, 14-23.

Krumbein, W. C. (1934), Size frequency distributions of sediments, *Journal of sedimentary Research*, *4*(2), 65-77.
Li, S., and R. E. Milliken (2016), An empirical thermal correction model for Moon Mineralogy Mapper data constrained by laboratory spectra and Diviner temperatures, *Journal of Geophysical Research: Planets*, *121*(10), 2081-2107.
Li, S., and R. E. Milliken (2017), Water on the surface of the Moon as seen by the Moon Mineralogy Mapper: Distribution, abundance, and origins, *Science advances*, *3*(9), e1701471.
Lock, S. J., S. T. Stewart, M. I. Petaev, Z. Leinhardt, M. T. Mace, S. B. Jacobsen, and M. Cuk (2018), The origin of the Moon within a terrestrial synestia, *Journal of Geophysical Research: Planets*, *123*(4), 910-951.
Longhi, J. (1992), Experimental petrology and petrogenesis of mare volcanics, *Geochimica et Cosmochimica Acta*, *56*(6), 2235-2251.
Longhi, J. (2006), Petrogenesis of picritic mare magmas: constraints on the extent of early lunar differentiation, *Geochimica et Cosmochimica Acta*, *70*(24), 5919-5934.
Lucey, P., R. Korotev, J. Gillis, L. Taylor, D. Lawrence, B. Campbell, R. Elphic, B. Feldman, L. Hood, and D. Hunten (2006), New views of the moon, *Rev. Mineral. Geochem*, 83-219.
McCubbin, F. M., A. Steele, E. H. Hauri, H. Nekvasil, S. Yamashita, and R. J. Hemley (2010a), Nominally hydrous magmatism on the Moon, *Proceedings of the National Academy of Sciences*, *107*(25), 11223-11228.
McCubbin, F. M., A. Steele, H. Nekvasil, A. Schnieders, T. Rose, M. Fries, P. K. Carpenter, and B. L. Jolliff (2010b), Detection of structurally bound hydroxyl in fluorapatite from Apollo Mare basalt 15058, 128 using TOF-SIMS, *American Mineralogist*, *95*(8-9), 1141-1150.
Milliken, R. E. (2006), *Estimating the water content of geologic materials using near-infrared reflectance spectroscopy: Applications to laboratory and spacecraft data*.
Milliken, R. E., and S. Li (2017), Remote detection of widespread indigenous water in lunar pyroclastic deposits, *Nature geoscience*, *10*(8), 561-565.
Milliken, R. E., and J. F. Mustard (2005), Quantifying absolute water content of minerals using near-infrared reflectance spectroscopy, *Journal of Geophysical Research: Planets*, *110*(E12).
Milliken, R. E., and J. F. Mustard (2007a), Estimating the water content of hydrated minerals using reflectance spectroscopy: I. Effects of darkening agents and low-albedo materials, *Icarus*, *189*(2), 550-573.
Milliken, R. E., and J. F. Mustard (2007b), Estimating the water content of hydrated minerals using reflectance spectroscopy: II. Effects of particle size, *Icarus*, *189*(2), 574-588.
Mueller, S. B., B. F. Houghton, D. A. Swanson, M. Poret, and S. A. Fagents (2019), Total grain size distribution of an intense Hawaiian fountaining event: case study of the 1959 Kīlauea Iki eruption, *Bulletin of Volcanology*, *81*(7), 43.
Rutherford, M. J., J. W. Head, A. E. Saal, E. Hauri, and L. Wilson (2017), Model for the origin, ascent, and eruption of lunar picritic magmas, *American Mineralogist: Journal of Earth and Planetary Materials*, *102*(10), 2045-2053.
Saal, A. E., E. H. Hauri, M. L. Cascio, J. A. Van Orman, M. C. Rutherford, and R. F. Cooper (2008), Volatile content of lunar volcanic glasses and the presence of water in the Moon's interior, *Nature*, *454*(7201), 192-195.
Saal, A. E., E. H. Hauri, J. A. Van Orman, and M. J. Rutherford (2013), Hydrogen isotopes in lunar volcanic glasses and melt inclusions reveal a carbonaceous chondrite heritage, *Science*, *340*(6138), 1317-1320.

836 Shearer, C., and J. Papike (1993), Basaltic magmatism on the Moon: A perspective from
837 volcanic picritic glass beads, *Geochimica et Cosmochimica Acta*, *57*(19), 4785-4812.
838 Shearer, C. K., P. C. Hess, M. A. Wieczorek, M. E. Pritchard, E. M. Parmentier, L. E. Borg, J.
839 Longhi, L. T. Elkins-Tanton, C. R. Neal, and I. Antonenko (2006), Thermal and magmatic
840 evolution of the Moon, *Reviews in Mineralogy and Geochemistry*, *60*(1), 365-518.
841 Watson, E., and J. Bender (1980), Diffusion of cesium, samarium, strontium, and chlorine in
842 molten silicate at high temperatures and pressures, paper presented at Geol. Soc. Am. Abstr.
843 Program.
844 Weitz, C. M., J. W. Head III, and C. M. Pieters (1998), Lunar regional dark mantle deposits:
845 Geologic, multispectral, and modeling studies, *Journal of Geophysical Research: Planets*,
846 *103*(E10), 22725-22759.
847 Wendlandt, R. F. (1991), Oxygen diffusion in basalt and andesite melts: experimental results and
848 discussion of chemical versus tracer diffusion, *Contributions to Mineralogy and Petrology*,
849 *108*(4), 463-471.
850 Wetzel, D. T., E. H. Hauri, A. E. Saal, and M. J. Rutherford (2015), Carbon content and
851 degassing history of the lunar volcanic glasses, *Nature Geoscience*, *8*(10), 755-758.
852 Wetzel, D. T., M. J. Rutherford, S. D. Jacobsen, E. H. Hauri, and A. E. Saal (2013), Degassing of
853 reduced carbon from planetary basalts, *Proceedings of the National Academy of Sciences*,
854 *110*(20), 8010-8013.
855 Wieczorek, M. A., G. A. Neumann, F. Nimmo, W. S. Kiefer, G. J. Taylor, H. J. Melosh, R. J.
856 Phillips, S. C. Solomon, J. C. Andrews-Hanna, and S. W. Asmar (2013), The crust of the Moon
857 as seen by GRAIL, *Science*, *339*(6120), 671-675.
858 Wilson, L. (1980), Relationships between pressure, volatile content and ejecta velocity in three
859 types of volcanic explosion, *Journal of Volcanology and Geothermal Research*, *8*(2-4), 297-313.
860 Wilson, L., and J. Head III (2003), Deep generation of magmatic gas on the Moon and
861 implications for pyroclastic eruptions, *Geophysical Research Letters*, *30*(12).
862 Wilson, L., and J. W. Head (2017), Generation, ascent and eruption of magma on the Moon:
863 New insights into source depths, magma supply, intrusions and effusive/explosive eruptions
864 (Part 1: Theory), *Icarus*, *283*, 146-175.
865 Wilson, L., and K. Keil (2012), Volcanic activity on differentiated asteroids: A review and
866 analysis, *Geochemistry*, *72*(4), 289-321.
867 Wilson, L., K. Keil, and T. J. McCOY (2010), Pyroclast loss or retention during explosive
868 volcanism on asteroids: Influence of asteroid size and gas content of melt, *Meteoritics &*
869 *Planetary Science*, *45*(8), 1284-1301.
870 Zhang, Y., and E. M. Stolper (1991), Water diffusion in a basaltic melt, *Nature*, *351*(6324), 306-
871 309.
872
873